Volume 4 | Number 11 | 21 March 2016 | Pages 3957–4322

Journal of Materials Chemistry A

Materials for energy and sustainability

www.rsc.org/MaterialsA

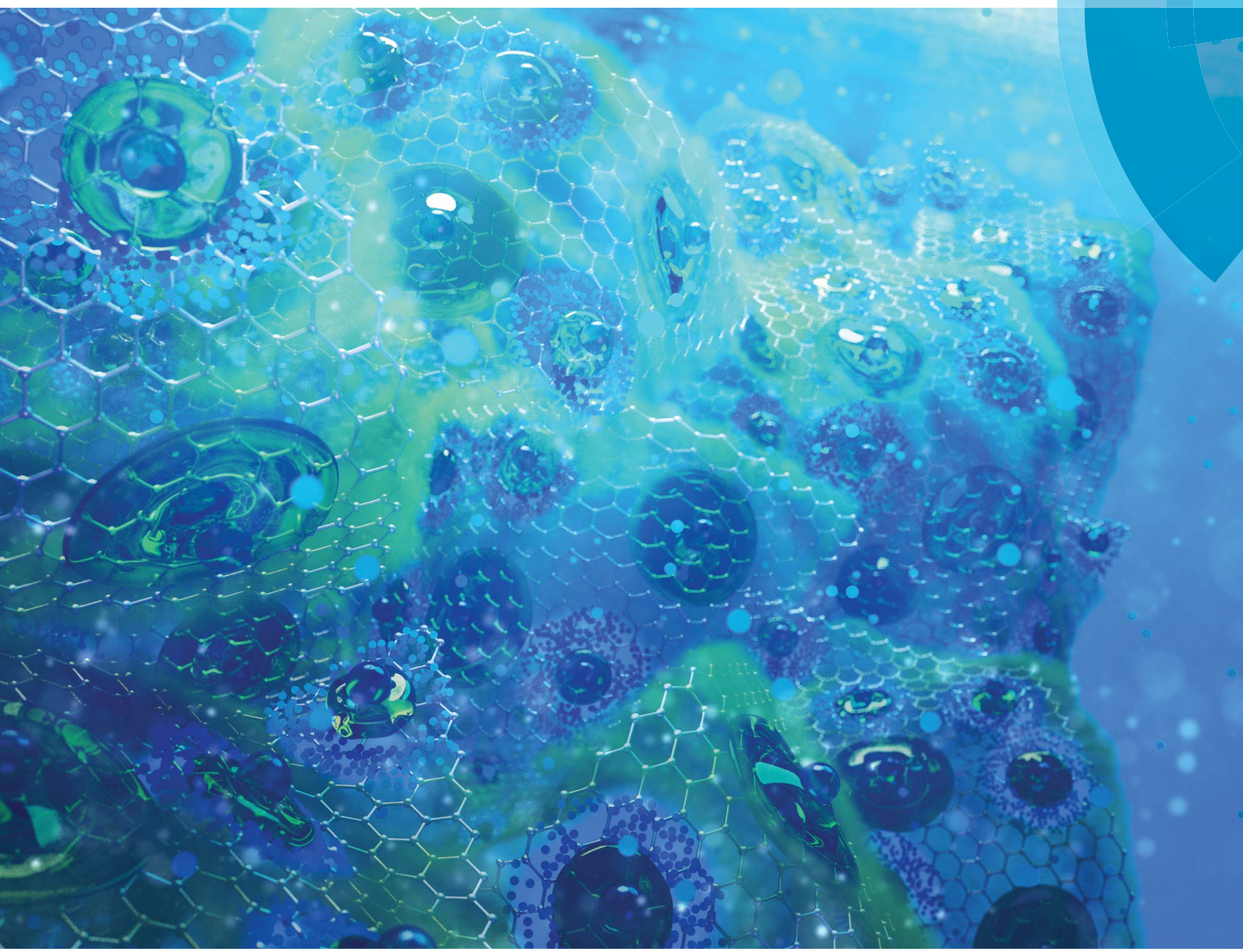

ISSN 2050-7488

ROYAL SOCIETY OF CHEMISTRY

PAPER

Y. Morris Wang *et al.*

Solvent-directed sol-gel assembly of 3-dimensional graphene-tented metal oxides and strong synergistic disparities in lithium storage

175 YEARS

Journal of Materials Chemistry A

PAPER

View Article Online
View Journal | View Issue

Cite this: J. Mater. Chem. A, 2016, 4, 4032

Solvent-directed sol-gel assembly of 3-dimensional graphene-tented metal oxides and strong synergistic disparities in lithium storage†

Jianchao Ye,‡[a] Yonghao An,‡[ab] Elizabeth Montalvo,[a] Patrick G. Campbell,[a] Marcus A. Worsley,[a] Ich C. Tran,[a] Yuanyue Liu,[ac] Brandon C. Wood,[a] Juergen Biener,[a] Hanqing Jiang,[c] Ming Tang[d] and Y. Morris Wang*[ab]

Received 30th December 2015
Accepted 8th February 2016

DOI: 10.1039/c5ta10730j

www.rsc.org/MaterialsA

Graphene/metal oxide (GMO) nanocomposites promise a broad range of utilities for lithium ion batteries (LIBs), pseudocapacitors, catalysts, and sensors. When applied as anodes for LIBs, GMOs often exhibit high capacity, improved rate capability and cycling performance. Numerous studies have attributed these favorable properties to a passive role played by the exceptional electronic and mechanical properties of graphene in enabling metal oxides (MOs) to achieve near-theoretical capacities. In contrast, the effects of MOs on the active lithium storage mechanisms of graphene remain enigmatic. *Via* a unique two-step solvent-directed sol-gel process, we have synthesized and directly compared the electrochemical performance of several representative GMOs, namely Fe_2O_3/graphene, SnO_2/graphene, and TiO_2/graphene. We observe that MOs can play an equally important role in empowering graphene to achieve large reversible lithium storage capacity. The magnitude of capacity improvement is found to scale roughly with the surface coverage of MOs, and depend sensitively on the type of MOs. We define a synergistic factor based on the capacity contributions. Our quantitative assessments indicate that the synergistic effect is most achievable in conversion-reaction GMOs (Fe_2O_3/graphene and SnO_2/graphene) but not in intercalation-based TiO_2/graphene. However, a long cycle stability up to 2000 cycles was observed in TiO_2/graphene nanocomposites. We propose a surface coverage model to qualitatively rationalize the beneficial roles of MOs to graphene. Our first-principles calculations further suggest that the extra lithium storage sites could result from the formation of Li_2O at the interface with graphene during the conversion-reaction. These results suggest an effective pathway for reversible lithium storage in graphene and shift design paradigms for graphene-based electrodes.

1. Introduction

Graphene–metal oxide (GMO) nanocomposites have attracted enormous attention for their potentials in energy storage and conversion,[1–11] including capacitors,[12] lithium-ion batteries (LIBs),[6–11,13] catalysis[2] (for fuel cells, water splitting, and air cleaning), and sensors. For the majority of these applications (*e.g.*, catalysis, sensing, capacitors), high surface-to-volume ratio nanoporous architectures such as those built from interconnected 3-dimensional (3D) graphene networks are preferable in order to maximize the potentials of both metal oxides and graphene.[14] For applications in LIBs, nanosized metal oxide (MO) particles and highly conductive graphene are considered beneficial for shortening Li^+-diffusion pathways and reducing ohmic polarization in the electrode,[15] leading to enhanced performance. In addition, porous space is critical in order to accommodate the relatively large volume expansion of many MOs upon lithiation. A vast number of studies have indeed demonstrated the effectiveness of these design principles. From the viewpoint of composite electrodes, however, there have been few attempts to optimize the pore space and maximize the exposure of MO active materials to electrolyte. For example, one popular approach involving graphene-wrapped GMOs structures[13,16] can easily lead to the inaccessibility of MOs to lithium-ions and inefficiently packed pore spaces. Perhaps because of the above reasons, the construction of many electrodes based on GMOs requires polymeric binders and/or carbon blacks, and has to be tested in an ultrathin geometry as thick electrodes

[a]Physical and Life Sciences Directorate, Lawrence Livermore National Laboratory, Livermore, CA 94550, USA. E-mail: ymwang@llnl.gov

[b]School for Engineering of Matter, Transport and Energy, Arizona State University, Tempe, AZ 85286, USA

[c]National Renewable Energy Laboratory, Golden, CO 80401, USA

[d]Department of Materials Science and Nano-Engineering, Rice University, Houston, TX 77005, USA

† Electronic supplementary information (ESI) available: Spherical-cap model, supporting Table S1, additional electrochemical performance and TEM measurements, and first-principles calculations (Fig. S1–S12). See DOI: 10.1039/c5ta10730j

‡ These authors contributed equally to this work.

could make more MOs inaccessible to electrolyte.[17] To this end, 3D GMO electrodes have certain advantages due to their binder free nature and ease of scale up to commercial LIB electrode thickness.

Although the current battery market is already dominated by carbon materials, especially graphite,[18] a fundamental question remains as to whether graphene could overtake graphite in terms of lithium storage capacity and long-term cycle stability. Many experiments have praised the enabling roles of graphene in LIBs.[19–22] However, both experiments[23] and theoretical calculations[24] indicate that defect-free graphene single sheets offer essentially zero lithium storage capacity, hinting at the critical relevance of graphene defects to lithium storage ability.[25,26] Existing experimental results of more disordered/defective graphene sheets have indeed revealed larger-than-graphite (~372 mA h g^{-1}) capacities;[27] but these values are not maintained for long cycles, challenging the reversibility of the underlying storage mechanisms. Critical issues remain as to whether isolated graphene sheets can afford sufficient Li storage sites and whether the storage mechanisms are fully reversible.[20,28–30] Intriguingly, very large capacities and superior cycle performance are achievable when similar graphene materials are applied to assemble GMO composites.[19,22,31] Even defect-free graphene is found to enhance both the capacity and rate-performance of GMOs[32] – a behavior that is in sharp contrast to the very poor performance of high quality graphene.[23] Nearly all studies[19,22,31–38] have attributed these outstanding properties of GMOs to the high intrinsic in-plane electrical conductivity, high mechanical strength, and chemical stability of graphene, which helps empower notoriously electrically insulating metal oxides (MOs) to achieve large theoretical capacities (~2–5 times higher than graphite) while simultaneously preventing MOs from agglomerating. In comparison, MOs are only considered beneficial for hindering graphene restacking and prolonging the cycle life of GMOs.[13,21] Most importantly, the total capacity achieved in some GMO nanocomposites is observed to be larger than the sum of each constitutive component – a synergistic effect that has not been fully understood in the literature.[19,33,39] One chief aim of our work is to investigate this interesting capacity synergistic effect. From the literature, the quantitative contribution of graphene to the overall capacities of GMOs and the related storage mechanisms remain highly controversial. For instance, it is unclear whether *this synergistic effect exists ubiquitously in all GMOs*, and whether *MOs affect graphene storage capacity*. The broad range of reported synthetic methods and wide variations in graphene quality (different defects and impurities)[26] make it nearly impossible to directly compare the performance of various GMOs. It remains challenging to elucidate the true origins of the synergistic mechanisms observed in some GMO systems.

In this work, we applied a two-step solvent-directed sol-gel method to prepare and compare electrochemical performance of various GMOs. Our approach has two unique advantages. First, since our sol-gel method dips prefabricated 3D porous graphene in metal ion solutions, all metal oxide nanoparticles appear to be anchored on the surface of graphene and are fully accessible to electrolyte (*i.e.*, open pore space). We thus refer to our approach as a solvent-directed sol-gel process. In essence, our approach helps to optimize the system-level performance by ensuring that most metal oxides are active, as our TEM examinations of lithiated samples do not reveal clear residual MO particles. Second, the approach can deposit most types of MOs onto the same prefabricated 3D graphene structure, allowing for direct comparison of electrochemical performance of a wide range of GMOs. Our approach chooses defective graphene, which not only offers lithium storage sites, but also facilitates the anchoring of MOs.[26] We report the experimental observations of large reversible lithium storage capacities of graphene sheets, enabled predominately by unheralded roles of MOs. Surprisingly we find that the magnitude of capacity contributions from graphene is mainly determined by active materials and the type of MO bound onto the graphene surface. Specifically, the lithium storage mechanisms of MOs (*i.e.*, conversion reaction, intercalation, conversion and alloying reaction) and their loading ratio *versus* graphene play key roles in determining graphene capacity contributions. Synergistic effects are chiefly observed in MOs with conversion reactions (Fe_2O_3 and SnO_2) but not in ion-intercalating oxides TiO_2. However, we found that TiO_2/graphene electrodes have substantially better long term cycle stability (up to 2000 cycles). We propose a surface coverage model to account for the unusual contribution of graphene to nanocomposites. Through first-principles calculations, we further suggest that the unique behavior of conversion-reaction MOs may be attributed to interfaces between Li_2O and graphene, which provide additional lithium storage sites and thus contribute to the high synergy between graphene and MOs. Our findings offer new insights on some longstanding controversies on the synergistic effects of GMOs and suggest a strategy for improving the effectiveness of graphene-based materials through hybridization with conversion-reaction MOs.

2. Experimental

Synthesis

To make meaningful comparison of capacity contributions from graphene for various GMOs, we have developed a two-step sol-gel method (see Scheme 1) to fabricate different types of nanocomposites that utilize the same prefabricated 3D graphene nanoporous structures (density ~70 mg cm^{-3}, surface area ~1500 m^2 g^{-1},[40] electrical conductivity ~2 S cm^{-1} with most sub-10 nm pores). The details of fabrication processes for 3D graphene structures have been reported in our previous work.[25,41,42] The Fe_2O_3/graphene was obtained by immersion of prefabricated 3D graphene in an ethanolic solution of Fe(III) salt (*e.g.* iron nitrate, iron chloride) to which an initiator (*e.g.* propylene oxide, trimethylene oxide) is added. Iron salt concentrations range from 0.05 to 1.4 M. Preferential nucleation of the nanoparticles on high surface area graphene can be achieved when the sol–gel chemistry is appropriately tuned. In our case, the molar ratio of initiator-to-Fe was set to 11 : 1 in order to promote nanoparticle nucleation and anchoring of FeOOH nanoparticles on the surface of graphene sheets, instead of in solution. After the particles have formed, the

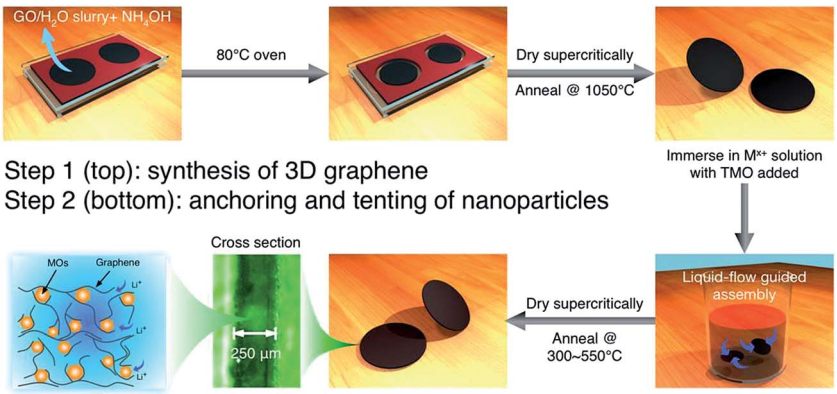

Scheme 1 A schematic illustration of the synthetic procedures for 3D porous MOs/graphene films (~250 μm thick). Step 1, three-dimensional graphene was fabricated by the reduction of graphene oxides using NH_4OH, supercritically dried, and annealed at 1050 °C in N_2 environment. Step 2, the MO nanoparticles were anchored inside 3D graphene by a sol–gel method, followed by additional supercritically-drying and annealing at 300–550 °C. The lower left schematic qualitatively shows the graphene-tented MOs structure formed by this approach.

coated 3D graphene was fired at 515 °C under nitrogen for 3 hours to convert FeOOH to Fe_2O_3 through a topotactic transition.

Similar solvent-directed dip coating techniques were used to deposit TiO_2 and SnO_2 particles on the 3D graphene. For the TiO_2 particles, the sol–gel was prepared *via* a two-step process involving acid-catalyzed hydrolysis of titanium(IV) ethoxide (1 g) using water (85.7 μl), hydrochloric acid (37%, 71.4 μl), and ethanol (3.57 g), followed by base-initiated gelation using propylene oxide (0.357 g). Calcination was done at 320 °C for 5 hours in air.

For the SnO_2/graphene, the sol–gel was prepared *via* an epoxide-initiated gelation method using tin chloride pentahydrate (0.56 g), trimethylene oxide (1.03 g), ethanol (7 g), and water (5 g).[43] No calcination was performed.

Structural characterizations

The phase and morphology of all hybrids were characterized by X-ray diffraction (XRD) (Bruker D8 Advance), field-emission scanning electron microscopy (SEM, JEOL 7401-F), and transmission electron microscopy (TEM, Philips CM300 FEG). The structures of 3D graphene and GMOs were also characterized by Raman spectroscopy (excitation wavelength: 633 nm, spot size: 0.8 μm, beam power: <1 mW). The pore volume and specific surface area were determined by nitrogen adsorption/desorption using the Brunauer–Emmett–Teller (BET) and Barrett–Joyner–Halenda (BJH) methods, with an ASAP 2020 surface area analyzer (Micromeritics Instrument Corp.). The samples for SEM observations were washed in dimethyl carbonate (DMC) for several hours, dried inside the glove box, and sealed in an argon-filled vial for transfer. It typically takes ~30 s for the vial to be opened and the sample was mounted in an SEM tab for investigations.

All TEM samples were prepared inside the glove box, which were washed in acetonitrile for more than 10 h, and dried inside the glove box for 5 h. A Lacey carbon coated TEM grid was directly pressed on top of a small piece of the hybrid sample, which was sealed tightly inside a vial and transferred to the TEM facility. It took about 15 s to open the vial and mount the sample on a TEM holder before it was inserted into TEM vacuum column for observation.

Electrochemical measurements

The 3D graphene and GMOs freestanding disks were used directly as the working electrodes without any carbon additives, polymer binders or current collectors. Lithium chips with a diameter of 5/16 inches and thickness of 0.01 inches were used as both reference and counter electrodes to construct a Swagelok-type half-cell. A commercial electrolyte (MTI Cor.) of 1 M $LiPF_6$ in a mixed solution of ethylene carbonate, diethyl carbonate and dimethyl carbonate (EC/DEC/DMC, v/v = 1 : 1 : 1) was adopted with a Celgard 3501 membrane as the separator. Cell assembly was conducted in argon-filled glove box (VAC Omni) with oxygen and water content less than 1 ppm. A Maccor 4304 battery cycler was used to perform cycling/data record within the voltage range of 0.01–3.0 V. The Macor system can be operated in both galvanostatic and potentiostatic modes. After electrochemical tests, cells were dissembled in a glove box and a small portion of the working electrodes were taken for further structural analysis.

3. Results and discussion

Structural and compositional analysis indicates that the as-synthesized 3D graphene has a Raman D-band to G-band ratio of ~1.4 (ESI, Fig. S1†), suggesting the disordered nature of 3D graphene. The transmission electron micrograph (TEM) in Fig. 1a confirms the defective nature with distorted ripples and roughened surface.[44] After 3D nanoporous graphene fabrication, various MOs (*e.g.*, Fe_2O_3, SnO_2, TiO_2, MnO_2, Co_2O_3) are anchored onto the internal surface of porous structures through a sol-gel method, which produces GMOs with a tented structure, Fig. 1b and Scheme 1. Micro- (<2 nm) and meso-pores (~2–50 nm) characterization before and after MO deposition indicate that the anchoring of nanoparticles has little influence

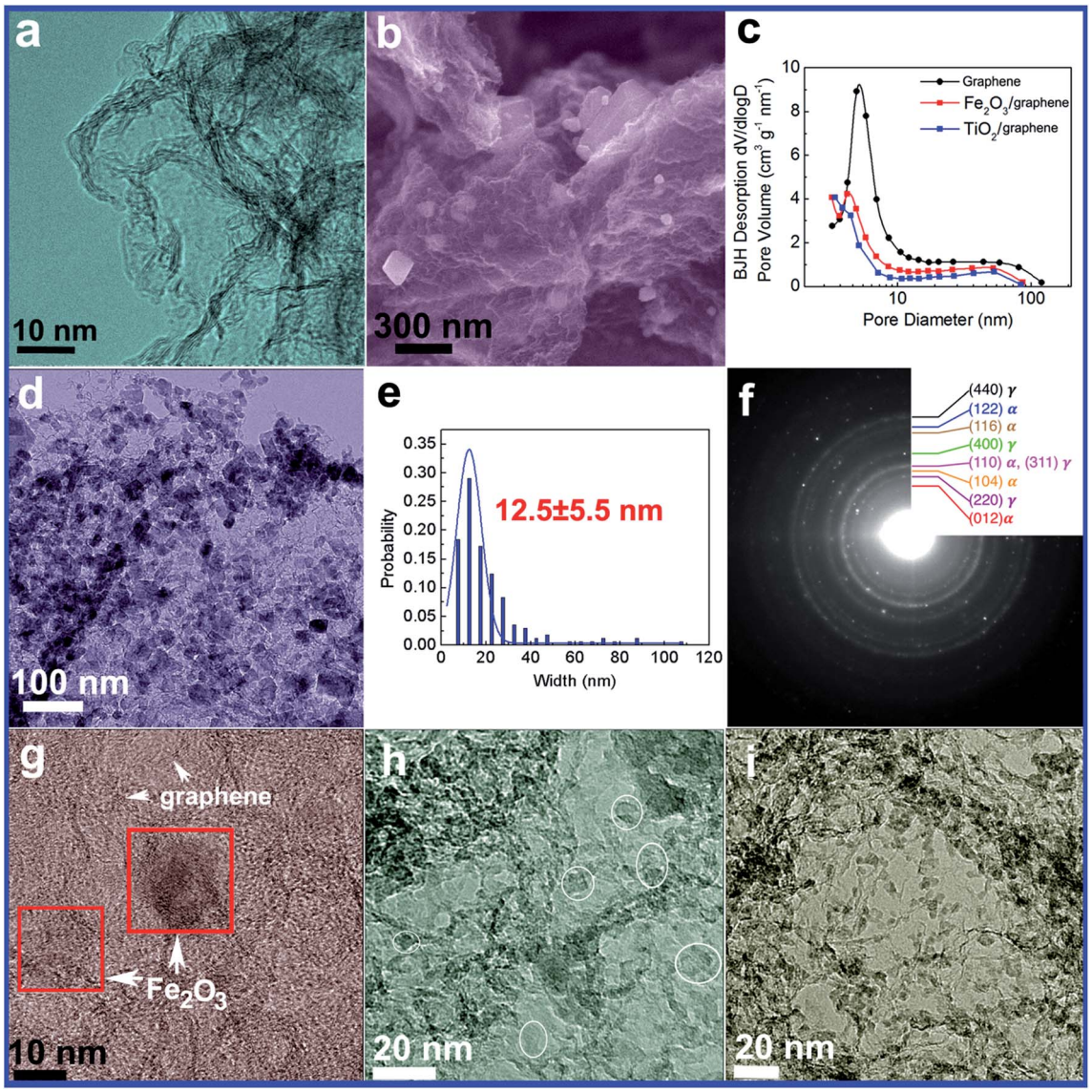

Fig. 1 Microstructure of the as-synthesized 3D graphene, Fe_2O_3/graphene, TiO_2/graphene, and SnO_2/graphene nanocomposites. (a) A bright-field TEM image of 3D graphene. (b) A SEM micrograph of Fe_2O_3/graphene hybrid. Sheet-like morphology of graphene is clearly visible. (c) Mesopores distribution inside hybrids before and after Fe_2O_3 and TiO_2 deposition. (d) A TEM image of Fe_2O_3/graphene. (e) Particle size distribution histogram of Fe_2O_3, as measured from a total count of 169 nanoparticles using a series of TEM images similar to the one shown in (d). (f) The selected area diffraction pattern of Fe_2O_3/graphene. (g) A high-resolution TEM image of Fe_2O_3/graphene, with two Fe_2O_3 nanoparticles accentuated inside squares (h) and (i), TEM images of as-synthesized TiO_2/graphene (anatase) and SnO_2/graphene, respectively. Some TiO_2 nanoparticles are highlighted with white cycles.

on the micropore distribution, Fig. 1c and ESI Fig. S2†; *i.e.*, most GMOs have similar pore-size distributions. Further TEM characterization (Fig. 1d), particle size histogram (Fig. 1e), and phase analysis indicate (Fig. 1f) that Fe_2O_3 (40 wt%) has a mixture of α- and γ-phases with an average particle size of $\sim 12.5 \pm 5.5$ nm. The faceted nature of Fe_2O_3 can be seen in the high-resolution TEM image shown in Fig. 1g. Pure γ-phase Fe_2O_3 tented inside 3D graphene with different loading ratios has also been synthesized in our work in order to perform parametric studies (ESI Fig. S3†). TiO_2 has an anatase phase with $\sim 5.5 \pm 0.6$ nm average particle size, Fig. 1h, whereas SnO_2 has an average particle size of 4.6 ± 0.5 nm, Fig. 1i; *i.e.*, the particle sizes of both TiO_2 and SnO_2 are well below 10 nm, helped by the constraint effect of graphene tent. Compared to other numerous GMO hybrids reported in the literature, our GMOs have the following characteristics that make them useful for the current studies: (1) all GMOs use the same pre-fabricated 3D graphene network (~ 250 μm thick); *i.e.*, the defect structures and pore distributions of graphene are similar for all hybrid GMOs. (2) The surface area and interface structures of our GMOs are comparable, as MOs are preferentially anchored on the open sites of 3D graphene pores. (3) All electrodes are additive- and binder-free. These structural similarities among all three types of MOs give us unique opportunities to compare

the electrochemical performance of various GMOs without the complications of other variables.

The electrochemical performance of three representative GMOs (namely, Fe_2O_3, SnO_2, and TiO_2) as anodes is investigated using a half-cell configuration. Although each of these GMOs nanocomposites has been studied before,[16,22,31,34,35,45,46] direct comparison of the performance of different MOs/graphene has not been possible due to the different synthesis routes used. The charging/discharging capacity at different rates shown in Fig. 2a indicates that pure 3D graphene shows relatively poor cycle performance, with lithiation capacity decreasing drastically as a function of cycle number. At a current density of 100 mA g^{-1}, the first discharge and charge capacities of graphene are 2603 mA h g^{-1} and 633 mA h g^{-1}, respectively, with a very low coulombic efficiency of ~24%. The discharge capacity rapidly drops below 850 mA h g^{-1} in the second cycle, and stabilizes at ~405 mA h g^{-1} (@100 mA g^{-1} current density) after 30 cycles. By comparison, Fe_2O_3/graphene (63 wt% Fe_2O_3) (Fig. 2b), SnO_2/graphene (63 wt% SnO_2) (Fig. 2c), and TiO_2/graphene (52 wt% TiO_2) (Fig. 2d) show far better cycle performance. For example, at a current density of 100 mA g^{-1} (*i.e.*, 0.1C if normalized against the Fe_2O_3 capacity of 1C = 1005 mA h g^{-1}), the Fe_2O_3/graphene sample exhibits a discharge capacity of ~1365 mA h g^{-1} (based on the total weight of the electrode) and a charge capacity of ~740 mA h g^{-1} at the first cycle, with a coulombic efficiency of ~54% (*i.e.*, significantly higher than that of graphene). The reversible capacity of Fe_2O_3/graphene stabilizes at a value of ~777 mA h g^{-1} at a current density of 100 mA g^{-1} after 30 cycles. For SnO_2/graphene, Fig. 2c, it has an initial coulombic efficiency of ~45% and the charge/discharge capacity is stabilized at ~747 mA h g^{-1} at a current density of 100 mA g^{-1} after 30 cycles. Again, these properties are superior to pure graphene. The initial coulombic efficiency of TiO_2/graphene is 31%, Fig. 2d, which remains higher than that of pure graphene. However, at 100 mA g^{-1} current density, the capacity of TiO_2/graphene is stabilized at 241 mA h g^{-1} after 30 cycles. The value of the TiO_2/graphene nanocomposite is in fact lower than that of pure graphene, presumably due to the low theoretical capacity of TiO_2 (Table 1). One important observation here is that our ultrathick (~250 μm), 3D graphene has enabled both electrically insulating (*i.e.*, Fe_2O_3 and TiO_2) and conductive (*i.e.*, SnO_2) MOs to achieve electrochemical performance without the need for polymeric binders. The authors caution a direct performance comparison of our MOs/graphene to those[6–8,35] reported in the literature without taking into account the electrode thickness and fabrication recipe used.

To quantitatively investigate and compare the potential synergistic effects between MOs and graphene, we use the rule-of-mixture to calculate the projected capacity ($C_{calculated}$) of each GMO by assuming that MOs exhibit the theoretical capacity shown in Table 1 and the graphene in the composite has the same measured capacity of the 3D nanoporous graphene shown in Fig. 2a. The weight ratios of MOs and graphene used in the calculation are measured from experiments. In the absence of any interference between MOs and graphene upon (de)lithiation, the capacity of a GMO should be no larger than $C_{calculated}$. We define a "synergistic factor" as $\delta = C_{measured}/C_{calculated} \times 100\%$, where $C_{measured}$ is the actual capacity measured from experiments at various charge/discharge rates. According to the definition of δ, when $\delta > 100\%$ we consider that a synergistic effect exists between graphene and MOs as the total capacity obtained in the nanocomposites is larger than

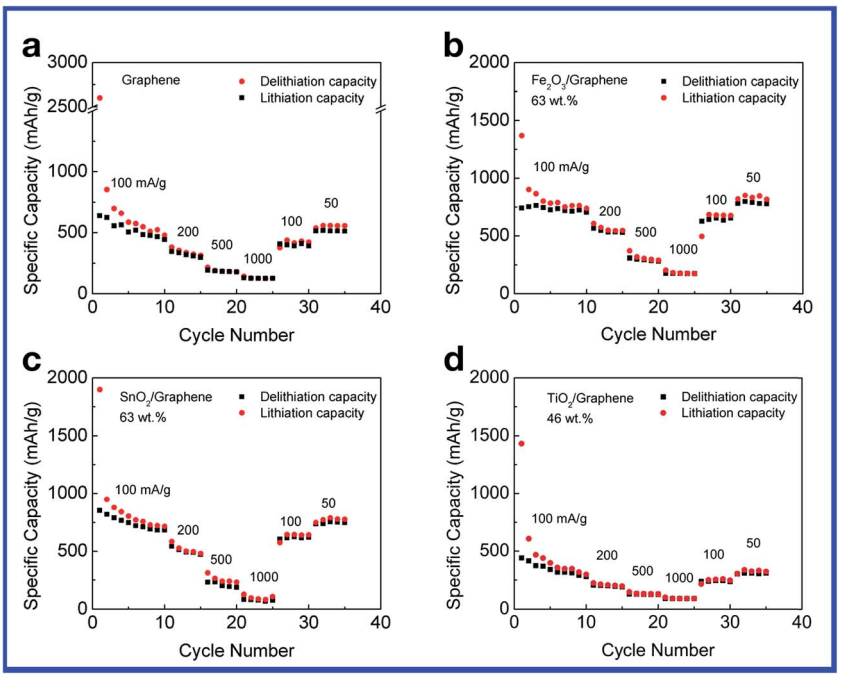

Fig. 2 Specific capacity, rate performance, and cycling stability of (a) 3D graphene, (b) Fe_2O_3/graphene, (c) SnO_2/graphene, and (d) TiO_2 (anatase)/graphene.

Table 1 Theoretical specific capacities (C), electrical conductivities (σ), and densities (ρ) of selected metal oxides as anode candidates for lithium-ion batteries. The order of metal oxides is sorted according to their C values, from high to low. The physical properties of Fe_2O_3, SnO_2, and TiO_2 used in this study are highlighted in bold[a]

Metal oxides	MnO_2	**Fe_2O_3**	Mn_3O_4	Fe_3O_4	Co_3O_4	MoO_2	**SnO_2**	NiO	CoO	CuO	V_2O_5	**TiO_2**
C (mA h g^{-1})	1231 (ref. 48 and 62)	**1005** (ref. 63)	935 (ref. 64)	924 (ref. 65)	889 (ref. 19)	837 (ref. 33)	**782**	716 (ref. 48)	714 (ref. 66)	673 (ref. 67)	294 (ref. 68)	**168** (ref. 69)
σ@RT[70] (S cm^{-1})	10^{-6} –10^{-3} (ref. 71)	**$\sim10^{-14}$ (α)[72] $\sim10^{-8}$ (γ)[73]**	$\sim10^{-15}$ (ref. 74)	$\sim10^{2}$	$\sim10^{-4}$	$\sim10^{-4}$	**2.5×10^{3}**	$\sim10^{-13}$	$\sim10^{-8}$	$\sim10^{-2}$	$\sim4 \times 10^{-2}$	**10^{-6}** (ref. 75)
ρ[70] (g cm^{-3})	5.03	**5.24 (α) 4.86–4.90 (γ)[76]**	4.7	5.00–5.40	6.07	6.47	**6.95**	7.45	5.70–6.70	6.40–6.45	3.36	**3.83 (anatase)**

[a] G. V. Samsonov, *Oxide Handbook*, New York, 2nd edn, 1982.

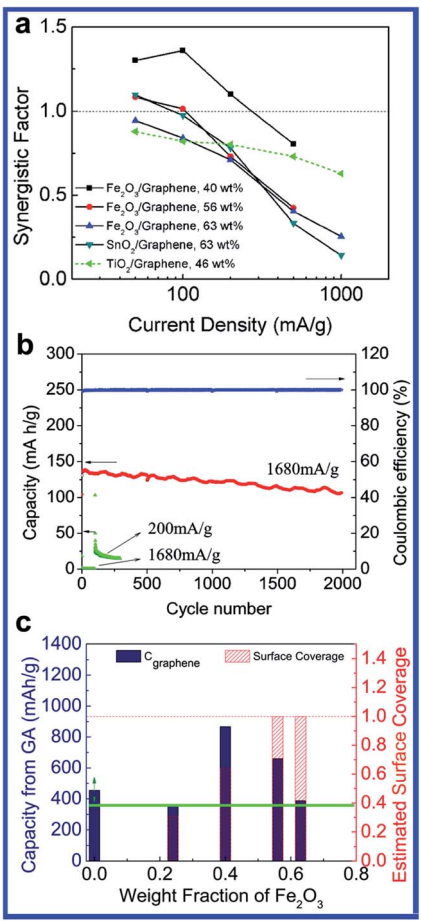

Fig. 3 Synergistic factors observed in three types of GMOs. (a) Measured synergistic factor as a function of charge current density for three MOs/graphene nanocomposites. Note that synergistic factor larger than 1.0 means the nanocomposites have synergistic effect. Otherwise, it has no synergistic effect between graphene and metal oxides. (b) Long-term cycle stability of TiO_2/graphene electrodes fabricated from our sol–gel methods. The anode was cycled in the voltage window of 1–3 V. The reference 3D graphene was also cycled in the same voltage window. (c) Quantitative capacity contribution from graphene when hybridized with Fe_2O_3 with different loading ratios. The estimated surface coverage is calculated according to the loading ratio of Fe_2O_3 *versus* graphene. The green solid line is a guide line of the capacity of pure graphene. The largest capacity contribution from graphene is observed when the loading ratio is at ~40–50 wt%.

the sum of each constitutive component contribution. It is apparent from Fig. 3a that both Fe_2O_3/graphene and SnO_2/graphene show a synergistic effect at low charging/discharging rates (≤100 mA g^{-1}). At higher charging/discharging rates, however, such a synergistic effect is not obvious likely due to the fact that the capacity of GMOs becomes limited by Li^+ transport in the electrolyte. TiO_2/graphene, on the other hand, exhibits little to no synergistic effect. At higher charging/discharging rates (≥200 mA g^{-1}), however, TiO_2/graphene has much better rate capacity as manifested by its rate-insensitive synergistic factor (green line) in Fig. 3a. Moreover, we find that intercalation-based TiO_2/graphene electrodes have outstanding long-term cycle stability and can be charged/discharged for more than 2000 cycles, whereas 3D graphene can only be cycled for less than 100 times, Fig. 3b. The long cycle performance of TiO_2/graphene could be due to its rather small volume expansion and the fact that it relies on intercalation mechanism that has anchored interfaces during the cycle. In contrast, conversion-reaction MOs have large volume expansion and constant changing interfaces during the cycling. Taken together, these results indicate that conversion-reaction MOs exhibit a synergistic effect when hybridized with graphene, albeit with rather sluggish (de)lithiation kinetics manifested by a sharp drop of capacity at higher charge/discharge rates. In contrast, the intercalation-based TiO_2 shows little synergistic effect but outstanding rate performance and cyclability. The excellent long-term cycling stability was recently also observed in TiO_2 coated nanoporous Au electrodes.[47]

To further elucidate the synergy in conversion-reaction MOs and graphene, we prepare a series of Fe_2O_3/graphene samples with four different loading ratios (24-, 40-, 56-, 63-wt% respectively) and estimate their respective graphene contributions at a current density of 50 mA g^{-1} after 30 cycles by subtracting the theoretical capacity of MOs, Fig. 3c. We observe graphene capacity contribution values of 391 mA h g^{-1}, 933 mA h g^{-1}, 709 mA h g^{-1}, and 422 mA h g^{-1} for these four loading ratios, respectively. By comparison, for pure graphene, we typically measured a capacity value of ~380–530 mA h g^{-1} at 50 mA g^{-1} after 30 cycles. Within the experimental error bar, this would suggest that two intermediate loading ratio samples show the strongest synergistic effect (*i.e.*, 40- and 56-wt% ones), whereas the synergistic effect is much weaker for the lowest- or the highest-loading-ratio sample. This behavior is surprising and

we suspect that it is related to the surface coverage of MOs on the graphene surface (to be discussed later).

To investigate the atomistic mechanisms of the synergistic effects by using Fe_2O_3/graphene as an example, we prepared transmission electron microscope (TEM) samples after multiple cycles inside the glove box and transferred them to the TEM holder using an argon (99.999+% purity) sealed vial. In order to better reveal the nanoparticle morphologies, the electrochemically cycled samples were washed in acetonitrile for more than 10 h. The microstructure of Fe_2O_3/graphene (56 wt% loading ratio) in both fully lithiated and delithiated states was investigated (after 30 cycles). Two sets of data were acquired independently, with the initial phase of Fe_2O_3 as either $\alpha + \gamma$ or pure γ. For the first set [*i.e.*, ($\alpha + \gamma$)-Fe_2O_3/graphene], we selectively chose a sample with few large nanoparticles (up to 110 nm) in order to investigate the possible particle-size effects. In the lithiated state, Fig. 4a, we find that almost all particles exhibit oval or circular shapes, with black-and-white contrast co-existing often within one single nanoparticle. The round geometries of the nanoparticles are in sharp contrast to the faceted particle-shapes seen in the as-synthesized state (see Fig. 1d and S4†). The agglomeration of nanoparticles is not evident in the lithiated state, demonstrating the effectiveness of graphene as a tent in separating nanoparticles. A zoomed-in TEM image shown in Fig. 4b reveals the existence of pure Fe nanoparticle surrounded by Li_2O, as suggested by the lower contrast of Li_2O and the crystalline morphology of Fe metal.[48] Under high-resolution TEM, lattice fringes are not readily visible for the Li_2O particles, suggesting the semi-amorphous nature of this phase.[49,50] The postmortem TEM examinations confirm the conversion reaction of Fe_2O_3. However, Li_2O crystallites are also found, two examples of which are shown in Fig. 4c. Both particles are identified to have the zone axis of <100>, as confirmed by the inset fast-Fourier transformation (FFT) pattern (*i.e.*, both areas have the identical FFT patterns) and diffraction pattern simulations (ESI Fig. S5†). Partially lithiated Fe_2O_3 particles can also be located (see ESI Fig. S6†); but this behavior seems to only occur in a few large Fe_2O_3 particles. This suggests that the (de) lithiation behavior of metal oxides is sensitive to their sizes and agglomerations – an observation that supports some earlier reports.[48] The incomplete (de)lithiation of nanoparticles may explain the low δ values in high-loading ratio GMOs. These interesting results accentuate the importance of using nano-sized metal oxide particles to maximize capacity for Li storage. We find that the round-shaped nanoparticles revert back to the faceted nanocrystals after they are fully delithiated, as confirmed by our TEM investigations (ESI Fig. S7†). The statistical particle size distribution after 30 cycles reveals insignificant change in average size (with a slightly larger standard deviation) (ESI, Fig. S8c†). This could be attributed to the excellent confinement effect of graphene sheets and the prevalent nanosized particles in our samples that are more resistant to pulverization compared to microsized counterparts.

Intriguingly, TEM studies further reveal the disappearance of α-phase for Fe_2O_3 after 30 cycles, as indicated by the SAD pattern (ESI Fig. S8†), which suggests that only γ-Fe_2O_3 remains. Furthermore, the SAD pattern no longer yields bright

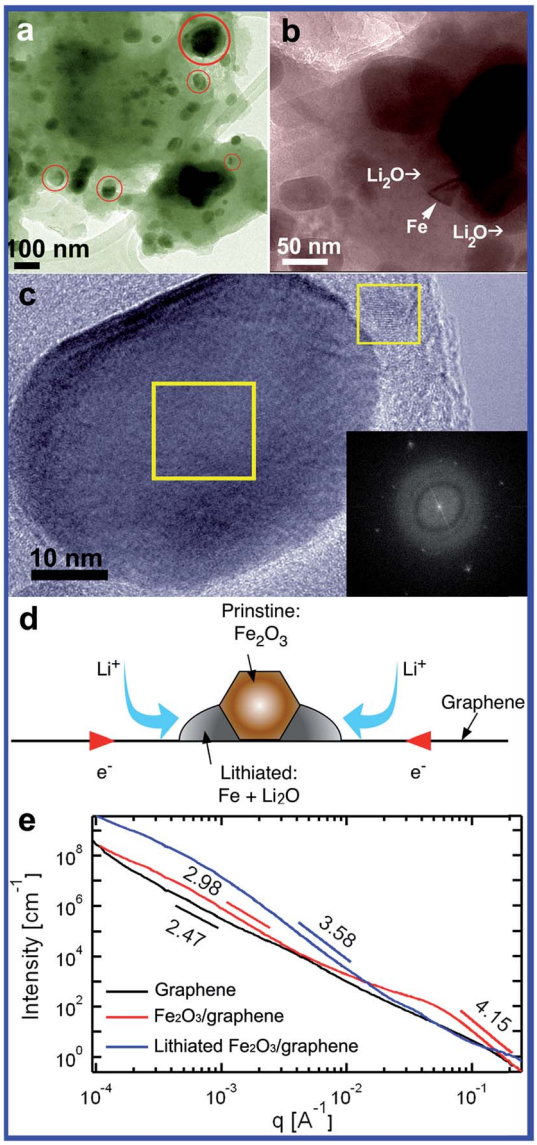

Fig. 4 Microstructure of Fe_2O_3/graphene after 30 cycles (in the lithiation state). (a) A low-magnification TEM image of Fe_2O_3/graphene. Some selected particles with black-and-white contrast are highlighted inside circles. (b) A zoomed-in TEM image of Fe_2O_3/graphene after lithiation. The areas representing Li_2O and Fe nanoparticles are pointed with white arrows. (c) A high-resolution TEM image of Li_2O particles. The inset fast-Fourier transformation (FFT) pattern is obtained from two square areas, which exhibit the same FFT pattern. (d) Schematic representation of the possible particle expansion mechanisms on graphene surface. (e) Background-corrected and slit-desmeared ultra-small angle X-ray scattering (USAXS) profiles obtained for three representative samples: (1) pristine 3D graphene (black curve); (2) pristine γ-Fe_2O_3/graphene (~56 wt% loading, red curve); and (3) lithiated γ-Fe_2O_3/graphene in (2). Power-law slopes are shown for the main scattering regions in each respective curve.

diffraction spots except for the continuous rings, indicating the disintegration of any pre-existing large particles or the transformation of single-crystalline to polycrystalline Fe_2O_3 particles upon long-term cycling. The preference of α-Fe_2O_3 transformation to more open cubic structure (*i.e.*, γ-Fe_2O_3) during the Li-ion intercalation is interesting,[51,52] and the γ-Fe_2O_3 was

also found not to revert back to the hexagonal α-Fe_2O_3 upon further cycling. Similar size-dependent stability crossovers between α-Fe_2O_3 and γ-Fe_2O_3 have been reported previously,[53] and can be attributed to the lower surface enthalpy of γ-Fe_2O_3. This structural irreversibility, however, does not seem detrimental to the electrochemical reversibility of our hybrid materials in short-term cycling, as we observe similar specific capacities for two comparison samples [see Table S1†, (α + γ)-Fe_2O_3 *vs.* γ-Fe_2O_3]. Previously, *in situ* TEM experiments have suggested that the delithiation product of Fe_2O_3 becomes FeO after the first cycle,[54] which is not observed in our work.

Another important yet intriguing observation from the TEM studies is that the average diameter of nanoparticles is observed to increase by more than a factor of 2.5 in the lithiated state (Table 2, and Fig. S9†). This would have projected an unrealistically large volume expansion of >1000% if nanoparticles were spherical and expanded uniformly during the lithiation. We observed this diameter change in both sets of samples that were examined under TEM. To resolve this apparent paradox between the measured particle sizes and the projected volume expansions, we performed further analysis by assuming a spherical-cap shape of particles that is consistent with the classical theory of heterogeneous nucleation on a flat surface (see ESI†). Our calculations suggest that nanoparticles do not retain a spherical shape upon lithiation, but rather are likely to change their aspect ratios and "spread" preferentially along the graphene/nanoparticles interfaces (*i.e.*, anchored interfaces), leading to pancake-like geometry that is supported by our TEM observations. Fig. 4d schematically illustrates the nanoparticles expansion process on the graphene sheet (also see Fig. S10†). We suspect that this unexpected particle shape change probably happens because the conversion reaction, which requires the participation of electrons, occurs preferentially on the graphene surface. Because electron transport within metal oxides (Fe_2O_3 and Li_2O) is extremely sluggish due to their poor conductivity, the reaction is kinetically favored to take place on the graphene surface, where electrons can easily reach the reaction front through facile transport within the graphene layer. In addition, ion species (*e.g.* Li^+ and O^{2-}) are likely to have larger mobilities along the solid/graphene or liquid/graphene interface than in the solid phases, further promoting the graphene surface as the preferred reaction site. Consequently, the reaction product (Li_2O + Fe) upon lithiation has a faster growth rate along the graphene sheets, which produces a significant change in the aspect ratio of the nanoparticles. Furthermore, the average Fe_2O_3 particle size in the delithiated state after 30 cycles measured from TEM images shows insignificant change from the as-synthesized state, indicating the reversibility of most particle shape changes.

Table 2 A summary of pristine and lithiated Fe_2O_3 particle sizes investigated in this study

Sample (wt%)	Pristine particle size	Lithiated particle size
α + γ-Fe_2O_3/graphene (56%)	~15 nm	48.9 ± 14.6 nm
α + γ-Fe_2O_3/graphene (40%)	12.5 ± 5.5 nm	—
γ-Fe_2O_3/graphene (56%)	8.1 ± 1.2 nm	20.6 ± 7.5 nm

Due to the destructive and 2D nature of the TEM technique, we further applied ultrasmall-angle X-ray scattering (USAXS) to probe the 3D shape change of γ-Fe_2O_3/graphene (56 wt%) electrodes. Fig. 4e presents the slit-desmeared USAXS data of the 3D graphene before and after deposition of Fe_2O_3, as well as of the lithiated Fe_2O_3/graphene. The USAXS of the pristine 3D graphene (black curve) shows two weak Guinier regions superimposed on an almost straight line with an overall power-law slope of ~2.5 that is consistent with two-dimensional-like structures comprising the graphene matrix. After deposition of Fe_2O_3 onto the graphene surface, the USAXS (red curve) instead exhibits two strong Guinier regions associated with two distinguishable distributions of scatterers. The first region occurs at a low scattering angle ($q < 3 \times 10^{-3}$ Å^{-1}) and has a power-law slope of 3.0 (from 10^{-3} Å^{-1} to 2×10^{-3} Å^{-1}), which is deviated from a slope of 2.5 for the GMA sample and is an indication for the modified (*i.e.*, thickening) GMA matrix upon deposition of Fe_2O_3. The second region is at a higher scattering angle ($q > 3 \times 10^{-3}$ Å^{-1}), with a power-law slope close to 4 from $q > 6 \times 10^{-2}$ Å^{-1}. Power law slopes of 4 generally occur at angles larger than those associated with the smallest scattering dimension, and often indicate 3-dimensional structures. In this case, the slope indicates these small structures are three-dimensional (*e.g.*, hemispherical particles) with smooth, sharp, and abrupt interfaces. In conjunction with the surface morphology, observed by SEM and TEM for the γ-Fe_2O_3/graphene sample, this region can be well ascribed to the scattering from Fe_2O_3 nanoparticles. Lithiation of Fe_2O_3/graphene induces substantial changes in the USAXS scattering profile. The Guinier associated with Fe_2O_3 nanoparticles reduces substantially, while the scattering intensity at lower q ($<2 \times 10^{-2}$ Å^{-1}) increases, suggesting a broadening of the mean particle size. A deviation of the power-law slope from −4 to −3.6 is observed, which is an evidence for the transformation of the structural shape from 3-dimensional nanoparticles to structures evolving towards 2-dimensional, or more disk-like for the lithiated Fe_2O_3. In addition, a new scattering region emerges at high q ($q > 10^{-1}$ Å^{-1}), which is indicative of the scattering from tiny structures (~1 nm) that did not exist before lithiation. This length scale is likely associated with Fe particles. The quantitative results extracted from USAXS agree with our TEM observations and support the abnormal particle shape changes seen in these hybrid materials.

Surface coverage model

The finding of the unexpected shape change of Fe_2O_3 nanoparticles upon (de)lithiation prompts us to propose a model to understand the synergistic effect observed in the Fe_2O_3/graphene and SnO_2/graphene hybrid electrodes. After multiple charge/discharge cycles, the total capacity of Fe_2O_3/graphene or SnO_2/graphene is substantially larger than the sum of two constitutive components, indicating that the GMO capacity derives from sources other than MOs. Besides MO nanoparticles, the capacity of hybrid electrodes could contain

contributions from binding to graphene and its structural defects, reactions between Li^+ and impurities (*e.g.*, residual oxygen), the formation of organic gel-like films, and/or Li^+ storage at interfaces. These contributions may account for the presence of multiple peaks and a large background on the differential capacity curves (Fig. S11†). While the detailed mechanisms of such auxiliary reactions remain to be clarified, it is plausible that they occur predominantly on the graphene surface because of easy access to electrons. However, a remarkable finding of this work is that these possible reactions only contribute significantly to reversible capacity in the presence of conversion-reaction nanoparticles. This fact provides valuable clues as to the probable origins of the synergistic effect.

It is well known that side reactions (*e.g.* electrolyte decomposition) cause SEI formation on the surface of battery anodes (*e.g.* graphite, silicon) during the first few cycles.[55,56] The large irreversible capacity seen in the pure graphene sample upon first discharge may be attributed to the formation of a stable SEI film on graphene surface. This SEI layer could be responsible for the very low reversible capacity in subsequent cycles by passivating the graphene surface and inhibiting the reversible reactions mentioned above, Fig. 5a. In the Fe_2O_3/graphene hybrid electrodes, however, we propose that the preferential expansion of nanoparticles on graphene sheets upon lithiation serves to cover the graphene surface and prevent SEI formation on the top while still allowing the reversible auxiliary reactions to occur forwardly, as illustrated in Fig. 5b. As the particles shrink during delithiation, the surface underneath is re-exposed to the electrolyte and becomes delithiated. The graphene surface around Fe_2O_3 nanoparticles can thus remain SEI-free upon cycling and contribute to the reversible capacity. This scenario is consistent with the persistent appearance of the graphene-related oxidation peaks (o2 and o5) on the differential capacity curves (Fig. S11†) and much higher coulombic efficiency observed in the hybrids than in pure graphene at the first cycle.

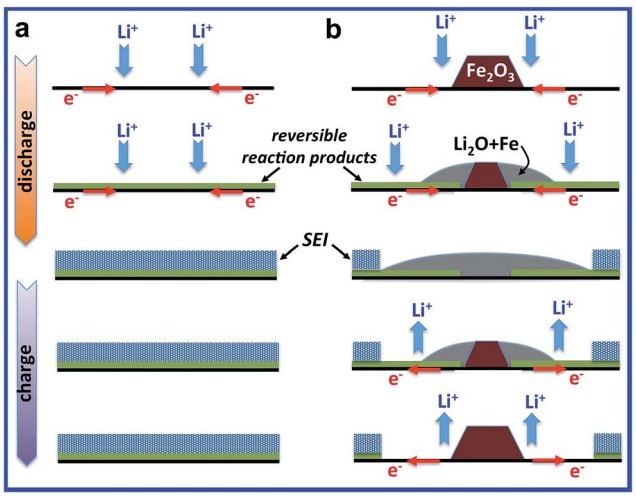

Fig. 5 Surface coverage model. (a) Schematics of solid-electrolyte-interphase (SEI) formation on graphene surface upon discharge and its effect on suppressing surface reactions that contribute to reversible Li storage capacity. (b) Schematics of the proposed mechanism for additional reversible capacity that is enabled by Fe_2O_3 particle expansion/shrinkage on top of the graphene surface.

To estimate the surface area "protected" by the nanoparticles, we measured the average particle size of a hybrid sample (56 wt% Fe_2O_3) consisting of only γ-Fe_2O_3 from TEM images, which has an average size of ~8.1 nm in the pristine state and ~20.6 nm in the lithiated state. Using these data and assuming that the pristine Fe_2O_3 particles have a hemispherical shape, calculations (ESI,† *Graphene surface coverage during the lithiation*) show that the nanoparticles will cover ~41% of the total graphene surface area in the lithiated state (up from 6% in the delithiated state). The actual coverage may be even higher considering that we use the upper limit of GA specific surface area (~1500 $m^2 g^{-1}$) in the calculation and the graphene sheets in our sample are highly curved and could make contact with Fe_2O_3 particles on multiple sides. Therefore, a large fraction of the graphene surface is covered by MOs upon lithiation so that the reversible auxiliary reactions can occur, which is consistent with the significant synergistic capacity enhancement seen in our hybrid samples. In contrast, the protection of graphene surface provided by the volume expansion of nanoparticles during lithiation does not exist in TiO_2/graphene because Li intercalation into TiO_2 causes little change in particle volume (~4%).[57] A significant and verifiable prediction from our hypothesis is that decreasing the particle size of metal oxides will lead to larger graphene-related reversible capacity, as the surface area covered by lithiated particles scales inversely with particle diameter (see more in ESI†). Based on the surface coverage model, the large volume expansion of conversion-reaction MOs helps surface protection from SEI and thus is beneficial for synergy.

First-principles simulations

Extra capacities have been observed in several conversion-reaction MOs, with the enhancements attributed to a variety of proposed mechanisms, including the existence of OH functional groups on MO surface,[58] the storage of lithium in the interface of metal particles and Li_2O,[59] and the formation of gel-like films.[60] However, these scenarios are equally applicable to pure MOs without graphene, and thus cannot be the origin of the observed improvements. The fact that very strong synergistic effects are observed only in conversion-reaction MOs but not in TiO_2/graphene points to a likely role played by Li_2O formed during lithiation. Our insights concerning the importance of surface coverage suggest that an interfacial phenomenon involving the graphene substrate might be the key to the process. Based on these observations, we propose that the formation of an interface between Li_2O and graphene during the lithiation process could play an important role to offer additional lithium storage sites. To test this hypothesis, we use first-principles calculations based on density functional theory to explore the possibility of lithium storage along the interface of Li_2O and graphene. The adsorption energy of Li is calculated as:

$$E_{ad} = E(\text{Li@host}) - E(\text{Li-atom}) - E(\text{host}) \quad (1)$$

where E(Li@host), E(Li-atom) and E(host) are the energy of the host with Li atom adsorption, and the energy of isolated systems, respectively. As shown in Fig. S12,† we find that Li cannot be stored on defect-free graphene or an exposed Li_2O surface because adsorption is energetically disfavored with respect to cohesion of bulk metallic Li. This result agrees with previous studies.[24,61] However, if Li_2O is instead formed at the interface with graphene, Li can be inserted at the interface with an E_{ad} that is favorable with respect to cohesion of bulk Li, meaning interface storage can be enabled. Moreover, we find that the new interfacial sites should be reversible, since E_{ad} lies only ~0.26 eV lower than the energy of bulk Li. Because this storage mechanism is interfacial in origin, it scales with the contact area between Li and the host, as we observe. In a certain regard, the enhancement is reminiscent of Li adsorption in graphite or bilayer graphene,[24] where two otherwise inactive graphene surfaces can create viable storage sites if they are interfaced. The pancake-like expansion of MOs observed in our TEM studies allows nanocomposites to form relatively large areas of Li_2O/graphene interfaces, providing additional sites for additional lithium storage. This mechanism has never been reported before but explains the strong loading-ratio-dependent synergy behavior of Fe_2O_3/graphene, which decreases as the surface coverage reaches saturation and access to the interfacial sites is reduced.

4. Conclusions

In summary, we have investigated the electrochemical behavior of three representative GMO nanocomposites made by a two-step solvent-directed sol-gel method. The unique advantage of our approach is to allow for the anchoring of most active MOs in the open pore space that is accessible by electrolyte. The GMOs have similar 3D graphene supporting structure, permitting direct comparison of MO effects on graphene storage capacities. Some main results of our work are summarized as follows:

(1) By using a newly defined synergistic factor, we find a strong synergistic effect between the MO and the 3D graphene host in conversation-reaction materials (*i.e.*, Fe_2O_3 and SnO_2) but not in intercalation-based TiO_2/graphene.

(2) For GMO nanocomposites, the graphene contribution to the total capacity not only depends upon the MO type, but also on the loading ratio of active materials in the graphene nanocomposites.

(3) In contrast to the popular belief, a pancake expansion behavior of MOs is observed in additive-free GMO electrodes.

(4) A surface coverage model is proposed to account for the unusual role of MOs in helping graphene to achieve large reversible capacities due to the buffeting of MOs to SEI formation.

(5) Our first-principles calculations for the first time suggest that formation of an interface between Li_2O and graphene may generate additional lithium storage sites that help to enhance the lithium storage capacity in conversion-reaction MOs. Our work offers mechanistic insights on the various synergistic effects of GMO nanocomposites.

Acknowledgements

Discussion with J. Lee, T. van Buuren, A. Wittstock, M. D. Merrill, and B. Sadigh is acknowledged. The work was performed under the auspices of the US Department of Energy by LLNL under contract No. DE-AC52-07NA27344. The project is supported by the Laboratory Directed Research and Development (LDRD) programs of LLNL (12-ERD-053). Y. L. acknowledges the support by US Department of Energy under Contract No. DE-AC36-08GO28308. The first-principles calculations were performed by using NREL Peregrine supercomputer, as well as LLNL CAB supercomputer. H. J. acknowledges the support from NSF CMMI-1067947 and CMMI-1162619. M.T. acknowledges support from DOE Office of Basic Energy Sciences Physical Behavior of Materials Program under grant number DE-SC0014435.

Notes and references

1 M. Armand and J. M. Tarascon, *Nature*, 2008, **451**, 652–657.
2 Y. Liang, Y. Li, H. Wang, J. Zhou, J. Wang, T. Regier and H. Dai, *Nat. Mater.*, 2011, **10**, 780–786.
3 J. B. Goodenough and Y. Kim, *Chem. Mater.*, 2010, **22**, 587–603.
4 Z.-S. Wu, G. Zhou, L.-C. Yin, W. Ren, F. Li and H.-M. Cheng, *Nano Energy*, 2012, **1**, 107–131.
5 J. Zai and X. Qian, *RSC Adv.*, 2015, **5**, 8814–8834.
6 S. Li, M. Ling, J. Qiu, J. Han and S. Zhang, *J. Mater. Chem. A*, 2015, **3**, 9700–9706.
7 J. Qiu, C. Lai, Y. Wang, S. Li and S. Zhang, *Chem. Eng. J.*, 2014, **256**, 247–254.
8 S. Li, Y. Wang, C. Lai, J. Qiu, M. Ling, W. Martens, H. Zhao and S. Zhang, *J. Mater. Chem. A*, 2014, **2**, 10211–10217.
9 L.-L. Xing, C.-H. Ma, C.-X. Cui and X.-Y. Xue, *Solid State Sci.*, 2012, **14**, 111–116.
10 X.-Y. Xue, C.-H. Ma, C.-X. Cui and L.-L. Xing, *Solid State Sci.*, 2011, **13**, 1526–1530.
11 L. Xing, C. Cui, C. Ma and X. Xue, *Mater. Lett.*, 2011, **65**, 2104–2106.
12 G. H. Yu, L. B. Hu, N. A. Liu, H. L. Wang, M. Vosgueritchian, Y. Yang, Y. Cui and Z. A. Bao, *Nano Lett.*, 2011, **11**, 4438–4442.
13 G. M. Zhou, D. W. Wang, F. Li, L. L. Zhang, N. Li, Z. S. Wu, L. Wen, G. Q. Lu and H. M. Cheng, *Chem. Mater.*, 2010, **22**, 5306–5313.
14 H.-K. Kim, S.-H. Park, S.-B. Yoon, C.-W. Lee, J. H. Jeong, K. C. Roh and K.-B. Kim, *Chem. Mater.*, 2014, **26**, 4838–4843.
15 Y. Gogotsi, *ACS Nano*, 2014, **8**, 5369–5371.
16 J. H. Sun, L. H. Xiao, S. D. Jiang, G. X. Li, Y. Huang and J. X. Geng, *Chem. Mater.*, 2015, **27**, 4594–4603.
17 Y. Gogotsi and P. Simon, *Science*, 2011, **334**, 917–918.
18 S. Stankovich, D. A. Dikin, G. H. B. Dommett, K. M. Kohlhaas, E. J. Zimney, E. A. Stach, R. D. Piner, S. T. Nguyen and R. S. Ruoff, *Nature*, 2006, **442**, 282–286.
19 Z. S. Wu, W. C. Ren, L. Wen, L. B. Gao, J. P. Zhao, Z. P. Chen, G. M. Zhou, F. Li and H. M. Cheng, *ACS Nano*, 2010, **4**, 3187–3194.

20 C. Hu, L. Lv, J. Xue, M. Ye, L. Wang and L. Qu, *Chem. Mater.*, 2015, **27**, 5253–5260.
21 D. Yoon, K. Y. Chung, W. Chang, S. M. Kim, M. J. Lee, Z. Lee and J. Kim, *Chem. Mater.*, 2015, **27**, 266–275.
22 X. Zhu, Y. Zhu, S. Murali, M. D. Stollers and R. S. Ruoff, *ACS Nano*, 2011, **5**, 3333–3338.
23 E. Pollak, B. S. Geng, K. J. Jeon, I. T. Lucas, T. J. Richardson, F. Wang and R. Kostecki, *Nano Lett.*, 2010, **10**, 3386–3388.
24 Y. Y. Liu, V. I. Artyukhov, M. J. Liu, A. R. Harutyunyan and B. I. Yakobson, *J. Phys. Chem. Lett.*, 2013, **4**, 1737–1742.
25 J. C. Ye, S. Charnvanichborikarn, M. A. Worsley, S. O. Kucheyev, B. C. Wood and Y. M. Wang, *Carbon*, 2015, **85**, 269–278.
26 J. Ye, M. T. Ong, T. W. Heo, P. G. Campbell, M. A. Worsley, Y. Liu, S. J. Shin, S. Charnvanichborikarn, M. J. Matthews, M. Bagge-Hansen, J. R. I. Lee, B. C. Wood and Y. M. Wang, *Sci. Rep.*, 2015, **5**, 16190.
27 D. Y. Pan, S. Wang, B. Zhao, M. H. Wu, H. J. Zhang, Y. Wang and Z. Jiao, *Chem. Mater.*, 2009, **21**, 3136–3142.
28 Y. Xu, Z. Lin, X. Zhong, B. Papandrea, Y. Huang and X. Duan, *Angew. Chem., Int. Ed.*, 2015, **54**, 5345–5350.
29 Y. Xu, Z. Lin, X. Zhong, X. Huang, N. O. Weiss, Y. Huang and X. Duan, *Nat. Commun.*, 2014, **5**, 4554.
30 T. Liu, K. C. Kim, R. Kavian, S. S. Jang and S. W. Lee, *Chem. Mater.*, 2015, **27**, 3291–3298.
31 J. Lin, Z. Peng, C. Xiang, G. Ruan, Z. Yan, D. Natelson and J. M. Tour, *ACS Nano*, 2013, **7**, 6001–6006.
32 K. H. Park, D. Lee, J. Kim, J. Song, Y. M. Lee, H. T. Kim and J. K. Park, *Nano Lett.*, 2014, **14**, 4306–4313.
33 Y. M. Sun, X. L. Hu, W. Luo and Y. H. Huang, *ACS Nano*, 2011, **5**, 7100–7107.
34 D. H. Wang, D. W. Choi, J. Li, Z. G. Yang, Z. M. Nie, R. Kou, D. H. Hu, C. M. Wang, L. V. Saraf, J. G. Zhang, I. A. Aksay and J. Liu, *ACS Nano*, 2009, **3**, 907–914.
35 B. Chen, H. Qian, J. Xu, L. Qin, Q.-H. Wu, M. Zheng and Q. Dong, *J. Mater. Chem. A*, 2014, **2**, 9345–9352.
36 Y. Chen, M. Zhuo, J. Deng, Z. Xu, Q. Li and T. Wang, *J. Mater. Chem. A*, 2014, **2**, 4449–4456.
37 M. Khan, M. N. Tahir, S. F. Adil, H. U. Khan, M. R. H. Siddiqui, A. A. Al-warthan and W. Tremel, *J. Mater. Chem.A*, 2015, **3**, 18753–18808.
38 J. Liu, W. Lv, W. Wei, C. Zhang, Z. Li, B. Li, F. Kang and Q.-H. Yang, *J. Mater. Chem. A*, 2014, **2**, 3031–3037.
39 G. Zhou, D.-W. Wang, L.-C. Yin, N. Li, F. Li and H.-M. Cheng, *ACS Nano*, 2012, **6**, 3214–3223.
40 Z. P. Chen, W. C. Ren, L. B. Gao, B. L. Liu, S. F. Pei and H. M. Cheng, *Nat. Mater.*, 2011, **10**, 424–428.
41 M. A. Worsley, S. O. Kucheyev, H. E. Mason, M. D. Merrill, B. P. Mayer, J. Lewicki, C. A. Valdez, M. E. Suss, M. Stadermann, P. J. Pauzauskie, J. H. Satcher, J. Biener and T. F. Baumann, *Chem. Commun.*, 2012, **48**, 8428–8430.
42 M. A. Worsley, T. T. Pham, A. Yan, S. J. Shin, J. R. I. Lee, M. Bagge-Hansen, W. Mickelson and A. Zettl, *ACS Nano*, 2014, **8**, 11013–11022.
43 T. F. Baumann, S. O. Kucheyev, A. E. Gash and J. H. Satcher, *Adv. Mater.*, 2005, **17**, 1546–1548.
44 M. S. Dresselhaus, A. Jorio, M. Hofmann, G. Dresselhaus and R. Saito, *Nano Lett.*, 2010, **10**, 751–758.
45 J. Sun, L. Xiao, S. Jiang, G. Li, Y. Huang and J. Geng, *Chem. Mater.*, 2015, **27**, 4594–4603.
46 J. Guo, H. Zhu, Y. Sun and X. Zhang, *J. Mater. Chem. A*, 2015, **3**, 19384–19392.
47 J. C. Ye, A. C. Baumgaertel, Y. M. Wang, J. Biener and M. M. Biener, *ACS Nano*, 2015, **9**, 2194–2202.
48 P. Poizot, S. Laruelle, S. Grugeon, L. Dupont and J. M. Tarascon, *Nature*, 2000, **407**, 496–499.
49 J. Y. Huang, L. Zhong, C. M. Wang, J. P. Sullivan, W. Xu, L. Q. Zhang, S. X. Mao, N. S. Hudak, X. H. Liu, A. Subramanian, H. Y. Fan, L. A. Qi, A. Kushima and J. Li, *Science*, 2010, **330**, 1515–1520.
50 Y. Liu, H. Zheng, X. H. Liu, S. Huang, T. Zhu, J. W. Wang, A. Kushima, N. S. Hudak, X. Huang, S. L. Zhang, S. X. Mao, X. F. Qian, J. Li and J. Y. Huang, *ACS Nano*, 2011, **5**, 7245–7253.
51 G. Jain, M. Balasubramanian and J. J. Xu, *Chem. Mater.*, 2006, **18**, 423–434.
52 D. Larcher, D. Bonnin, R. Cortes, I. Rivals, L. Personnaz and J. M. Tarascon, *J. Electrochem. Soc.*, 2003, **150**, A1643–A1650.
53 A. Navrotsky, L. Mazeina and J. Majzlan, *Science*, 2008, **319**, 1635–1638.
54 Q. Su, D. Xie, J. Zhang, G. Du and B. Xu, *ACS Nano*, 2013, **7**, 9115–9121.
55 E. Peled, in *Lithium Batteries*, ed. J. P. Gabano, Academic Press, New York, 1983, ch. 3, p. 43.
56 P. Arora, R. E. White and M. Doyle, *J. Electrochem. Soc.*, 1998, **145**, 3647–3667.
57 Z. Yang, D. Choi, S. Kerisit, K. M. Rosso, D. Wang, J. Zhang, G. Graff and J. Liu, *J. Power Sources*, 2009, **192**, 588–598.
58 Y.-Y. Hu, Z. Liu, K.-W. Nam, O. J. Borkiewicz, J. Cheng, X. Hua, M. T. Dunstan, X. Yu, K. M. Wiaderek, L.-S. Du, K. W. Chapman, P. J. Chupas, X.-Q. Yang and C. P. Grey, *Nat. Mater.*, 2013, **12**, 1130–1136.
59 Y. F. Zhukovskii, P. Balaya, E. A. Kotomin and J. Maier, *Phys. Rev. Lett.*, 2006, **96**, 058302.
60 A. Ponrouch, P.-L. Taberna, P. Simon and M. Rosa Palacin, *Electrochim. Acta*, 2012, **61**, 13–18.
61 Y. Liu, Y. M. Wang, B. I. Yakobson and B. C. Wood, *Phys. Rev. Lett.*, 2014, **113**, 028304.
62 A. L. M. Reddy, M. M. Shaijumon, S. R. Gowda and P. M. Ajayan, *Nano Lett.*, 2009, **9**, 1002–1006.
63 J. Chen, L. N. Xu, W. Y. Li and X. L. Gou, *Adv. Mater.*, 2005, **17**, 582–586.
64 H. L. Wang, L. F. Cui, Y. A. Yang, H. S. Casalongue, J. T. Robinson, Y. Y. Liang, Y. Cui and H. J. Dai, *J. Am. Chem. Soc.*, 2010, **132**, 13978–13980.
65 W. M. Zhang, X. L. Wu, J. S. Hu, Y. G. Guo and L. J. Wan, *Adv. Funct. Mater.*, 2008, **18**, 3941–3946.
66 C. H. Chen, B. J. Hwang, J. S. Do, J. H. Weng, M. Venkateswarlu, M. Y. Cheng, R. Santhanam, K. Ragavendran, J. F. Lee, J. M. Chen and D. G. Liu, *Electrochem. Commun.*, 2010, **12**, 496–498.
67 J. Morales, L. Sanchez, F. Martin, J. R. Ramos-Barrado and M. Sanchez, *Electrochim. Acta*, 2004, **49**, 4589–4597.

68 A. M. Cao, J. S. Hu, H. P. Liang and L. J. Wan, *Angew. Chem., Int. Ed.*, 2005, **44**, 4391–4395.
69 L. Kavan, M. Gratzel, J. Rathousky and A. Zukal, *J. Electrochem. Soc.*, 1996, **143**, 394–400.
70 G. V. Samsonov, *The Oxide Handbook*, IFI/Plenum, New York, 2nd edn, 1982.
71 J. M. Ko and K. M. Kim, *Mater. Chem. Phys.*, 2009, **114**, 837–841.
72 F. J. Morin, *Phys. Rev.*, 1951, **83**, 1005–1010.
73 A. K. Nikumbh, P. L. Sayanekar and M. G. Chaskar, *J. Magn. Magn. Mater.*, 1991, **97**, 119–125.
74 E. M. Logothetis and K. Park, *Solid State Commun.*, 1975, **16**, 909–912.
75 L. F. Shen, X. G. Zhang, H. S. Li, C. Z. Yuan and G. Z. Cao, *J. Phys. Chem. Lett.*, 2011, **2**, 3096–3101.
76 Those density data are from JCPDS cards: PDF#00-033-0664 and PDF#00-039-1346.